Effects of magnetic field on the turbulent wake of a cylinder in free-surface magnetohydrodynamic channel flow

John R. Rhoads[1,†], Eric M. Edlund[2] and Hantao Ji[1,2]

[1]Department of Astrophysical Sciences, Princeton University, Princeton, NJ 08544, USA

[2]Princeton Plasma Physics Laboratory, Princeton, NJ 08543, USA

Results from a free-surface magnetohydrodynamic (MHD) flow experiment are presented detailing the modification of vortices in the wake of a circular cylinder with its axis parallel to the applied magnetic field. Experiments were performed at Reynolds numbers of the order of $Re \sim 10^4$ as the interaction parameter N, representing the ratio of electromagnetic forces to inertial forces, was increased through unity. The von Kármán vortex street in the wake of the cylinder was observed by simultaneously sampling the gradient of the induced electric potential, $\nabla\phi$, at 16 cross-stream locations as a proxy for the streamwise fluid velocity. An ensemble of vortex velocity profiles was measured as a function of the applied magnetic field strength. Results indicate a significant change in the circulation of vortices and the deviations from the average profile as N was increased. By sampling the fluctuations in $\nabla\phi$ at three locations in the wake, the decay of the vortices was examined and the effective viscosity was found to decrease as $N^{-0.49\pm0.04}$. Using temperature as a passive tracer, qualitative observations were made with an infrared (IR) camera that showed significant changes in the wake, including the absence of small-scale structures at high magnetic field strengths. Collectively, the results suggest that the reduction in effective viscosity was due to the suppression of the small-scale eddies by the magnetic field. The slope of the power spectrum was observed to change from a $k^{-1.8}$ power law at low N to a $k^{-3.5}$ power law for $N > 1$. Together, these results suggest the flow smoothly transitioned from a hydrodynamic state to a magnetohydrodynamic regime over the range of $0 < N < 1$.

Key words: MHD and electrohydrodynamics, MHD turbulence, vortex dynamics

1. Introduction

Studying the flow past a cylinder is a classical experiment used to investigate the transition to turbulence. However, in electrically conducting fluids, turbulent structures can change dramatically in the presence of a magnetic field due to the fluid's ability to support internal currents. Experiments described in this paper investigated the transition that occurred in the wake of an obstruction as a magnetic field was applied while holding the fluid velocity constant.

† Email address for correspondence: jrhoads@pppl.gov

The experiments presented in this work considered magnetohydrodynamic (MHD) flows with a Reynolds number $Re = v_\infty L / \nu > 8000$, where v_∞ is the free-stream fluid velocity, L is the cylinder diameter and ν is the kinematic viscosity. This value of Re falls into what is commonly referred to as the shear-layer transition regime for hydrodynamic flows (pp. 489, 520–524 Williamson 1996). In this regime, the wake retains many of the features present in a von Kármán street, which evolves at lower Reynolds numbers ($Re = 50$–200) before the transition to turbulence. However, in the shear-layer transition regime, the discrete, alternating vortices of the von Kármán street become localized regions of vorticity, with small-scale three-dimensional turbulent features superimposed on larger vortex structures with a size of the order of the obstruction diameter (Wei & Smith 1986; Williamson, Wu & Sheridan 1995). Excellent visualizations of both laminar and turbulent von Kármán streets are included by Van Dyke (1982, pp. 31, 56–57). As a matter of convention, the larger regions of circulation are referred to as 'vortices' in this paper, which may in turn contain smaller-scale 'eddies' due to the turbulent nature of the flow.

While small-scale three-dimensional eddies are expected for a hydrodynamic flow in this turbulent regime, the addition of a magnetic field introduces anisotropic damping to the fluid motion via ohmic dissipation. In particular, eddies with vorticity misaligned with the applied magnetic field, $\boldsymbol{B}$, experience a torque resulting from the interaction of induced currents with the magnetic field, while eddies initially aligned with $\boldsymbol{B}$ elongate along the magnetic field lines (pp. 122–132 Davidson 1997, 2001). By restricting fluid motion, the magnetic field causes the flow to become quasi-two-dimensional (see Alemany *et al.* 1979; Klein & Pothérat 2010), thereby affecting the energy cascade as proposed by Kolmogorov and others for hydrodynamic systems (Kolmogorov 1941; Kraichnan 1967, 1971; Frisch 1995). In this work, the transition from a three-dimensional flow to a more quiescent MHD flow was observed to be a smooth function of the strength of the applied magnetic field.

Beginning with the work of Strouhal (1878), flow separation of the fluid as it moves past an object has been studied extensively over a wide range of both geometries and Reynolds numbers in the laboratory (see Williamson 1996). The majority of these studies have focused on hydrodynamic behaviour, although some work has examined MHD flows. Several experimental groups investigating MHD flows made point measurements in the wake behind a cylinder in various geometries to study the fluctuation levels in addition to the shedding mechanism and shape of the wake (Kolesnikov & Tsinober 1972; Papailiou & Lykoudis 1974; Lahjomri, Capéran & Alemany 1993; Branover *et al.* 2004). Experiments have also been conducted in a duct-flow geometry using an array of probes at the wall to observe structures in the wake of a cylinder (Frank, Barleon & Müller 2001). However, these results did not include detailed measurements of the internal velocity structure of the vortices. The results presented in this paper complement prior work by measuring the internal velocity profile of vortices, which provides insight into the behaviour of MHD turbulence.

Knaepen & Moreau (2008) provide an excellent review of the literature regarding low-R_m (magnetic Reynolds number), quasi-two-dimensional systems that are created through the anisotropic ohmic dissipation described above. Several groups experimentally and/or theoretically investigated this phenomenon by artificially driving turbulent-like states over a wide range in both Hartmann numbers and interaction parameters (Kolesnikov & Tsinober 1974; Alemany *et al.* 1979; Sommeria & Moreau 1982; Sommeria 1986; Zikanov & Thess 1998; Alboussière, Uspenski & Moreau 1999; Tabeling 2002; Thess & Zikanov 2007; Klein, Pothérat & Alferenok 2009;

Klein & Pothérat 2010). Yet, once again, the internal velocity profile of the vortices within a turbulent wake was not addressed. Sreenivasan & Alboussière (2002) studied the decay of an artificially created vortex subjected to an axial magnetic field and found that, for $N \gg 1$, the MHD forces arising from induced currents within the flow dominate the damping of the vortex and render viscous dissipation almost entirely negligible. However, Sreenivasan & Alboussière (2002) did not report detailed measurements for the transition that occurs between $0 < N \lesssim 2$ as the flow loses many of its hydrodynamics characteristics, which is the regime at the focus of this work.

Several groups have worked on experimental and computational modelling of the wake behind a bluff body in MHD flow, including some work on the transition between hydrodynamic and MHD regimes. In particular, Branover *et al.* (2004, p. 294) made point measurements behind a rectangular obstruction in duct flow and found that the mean flow in the wake underwent a transition in the range $0.5 < N < 1$. Mück *et al.* (2000, p. 279) performed three-dimensional MHD simulations of a similar geometry with a circular cylinder, showing the collimation of shed vortices at a moderate Reynolds number of 250 and indicating a clear transition to a two-dimensional state somewhere in the range $0.2 \leqslant N \lesssim 1$. Dousset & Pothérat (2008) presented simulation results of the flow past a cylinder at high Hartmann number. Although the shedding frequency that they found qualitatively agrees, the behaviour of the shed vortices varied considerably from the results presented in this paper. Dousset & Pothérat (2012) and Andreev, Kolesnikov & Thess (2013) also performed simulations and experiments (respectively) with a truncated cylinder that showed the stabilizing effect of a magnetic field on three-dimensional horseshoe vortices.

Most recently, Kanaris *et al.* (2013) performed time-dependent fully three-dimensional direct numerical simulations of liquid metal flow around a cylinder in a duct geometry with an applied magnetic field parallel to the axis of the cylinder. In addition to investigating the critical Reynolds number for the onset of vortex shedding as a function of the interaction parameter, Kanaris *et al.* also showed evidence for the quasi-two-dimensionalization of the wake of the cylinder at higher applied field intensities. In particular, they show the suppression of three-dimensional eddies as vortices are advected downstream around $N \simeq 1$. The suppression of these smaller-scale features results in a more coherent and longer-lived vortex street consisting of nearly cylindrical vortices. Direct quantitative comparison of the internal velocity profiles of the vortices presented in this paper with computational results was not available.

Klein & Pothérat (2010) experimentally investigated this regime between hydrodynamic and quasi-two-dimensional behaviour with a driven vortex and observed a smooth transition in correlation measurements made to quantify the three-dimensionality of their system. For their work, Klein & Pothérat (2010) defined a local interaction parameter for a given structure being driven. However, owing to the dynamic nature of the vortices considered in this work, the interaction parameter is calculated solely on the mean fluid velocity in the wake and the fluid depth in the same way as Thess & Zikanov (2007) addressed the issue. By characterizing the flow with a global N, these results focus on the effects of the magnetic field on three-dimensional structures created as the fluid separates from the cylinder and interacts with the boundary layer at the bottom of the flow, rather than those that would be created due to the rotational motion of the vortex itself. The vortices are then taken to be evolving entities within a repeatable framework characterized by the global interaction parameter.

The work presented here focuses on the transitions that were observed in vortex velocity profiles, fluctuation spectra and the effective viscosity as the interaction

parameter was increased past unity. The flow was observed to transition smoothly from a turbulent hydrodynamic state into a more quiescent state as N was increased. In the following sections, the techniques used to quantify this transition will be discussed.

2. Background

The introduction of an external magnetic field requires an additional term in the Navier–Stokes equations to describe the body force resulting from induced currents within the fluid. For closure, Ohm's law, Faraday's law and Ampere's law must also be included along with the incompressibility condition. That is

$$\rho \left(\frac{\partial \boldsymbol{v}}{\partial t} + (\boldsymbol{v} \cdot \nabla) \, \boldsymbol{v} \right) = -\nabla p + \mu \nabla^2 \boldsymbol{v} + \boldsymbol{j} \times \boldsymbol{B}, \tag{2.1}$$

$$\boldsymbol{j} = \sigma (\boldsymbol{E} + \boldsymbol{v} \times \boldsymbol{B}), \tag{2.2}$$

$$\nabla \times \boldsymbol{E} = 0, \tag{2.3}$$

$$\nabla \times \boldsymbol{B} = \mu_0 \, \boldsymbol{j}, \tag{2.4}$$

$$\nabla \cdot \boldsymbol{B} = 0 \quad \text{and} \quad \nabla \cdot \boldsymbol{v} = 0, \tag{2.5}$$

where ρ is the fluid density, $\boldsymbol{v}$ is the velocity, p is the pressure, μ is the dynamic viscosity, $\boldsymbol{j}$ is the current density, $\boldsymbol{B}$ is the magnetic field, σ is the conductivity of the fluid, $\boldsymbol{E}$ is the electric field and μ_0 is the magnetic permeability of the fluid. The effects of the induced magnetic field are negligible ($\partial \boldsymbol{B}/\partial t \approx 0$) when $R_m = \mu_0 \sigma v_\infty h \ll 1$, where h is the fluid depth. In this 'inductionless' regime, electric fields can be expressed as purely electrostatic, as seen in (2.3), and a scalar potential ($\boldsymbol{E} = -\nabla \phi$) can be introduced. For experiments presented in this paper, $R_m < 10^{-2}$. The displacement current has also been neglected in Ampere's law, (2.4), giving rise to a solenoidal current density ($\nabla \cdot \boldsymbol{j} = 0$).

As the strength of the applied magnetic field is increased, the electromagnetic contribution to the Navier–Stokes equations plays a greater role in determining the dynamics of the flow. The ratio of the contribution of the electromagnetic term to the inertial term in (2.1) is often referred to as the interaction parameter (also called the Stuart number), N. Similarly, the ratio of electromagnetic forces to viscous forces is defined as the square of the Hartmann number, Ha, as shown in table 1. In this work, the characteristic length, L, is defined as the cylinder diameter d, v_0 is defined as the mean fluid velocity in the wake, v_∞ is defined as the free-stream fluid velocity and B_0 is defined as the magnitude of the applied magnetic field. For Ha and R_m, h is taken to be the fluid depth due to the geometry of the experiment. The free-stream velocity, v_∞, was used to calculate the Reynolds number, since the shear in the flow created by the fluid passing the obstacle dictates the nature of the turbulence in the wake. The interaction parameter was calculated using the wake velocity, v_0, since the dynamics of the vortices were more directly affected by the velocity behind the cylinder as opposed to the free-stream velocity.

In addition to examining the change in the velocity profile at a given location in the wake as a function of the applied magnetic field, this work also focused on the evolution and dissipation of vortices as they were advected downstream. It is proposed and discussed in §4.3 that this dissipation takes the form of a diffusive process governed by an 'effective viscosity'. Viscous dissipation causes the velocity of a stationary (or non-advecting) vortex to evolve according to

$$\frac{\partial \boldsymbol{v}}{\partial t} = \nu \nabla^2 \boldsymbol{v}, \tag{2.6}$$

Magnetic Reynolds number	R_m	$= \mu_0 \sigma v_\infty h$	Ratio of magnetic advection to diffusion
		$= Re \dfrac{\nu}{\lambda}$	Magnetic diffusivity, $\lambda = 1/\mu_0 \sigma$
Reynolds number	Re	$= \dfrac{v_\infty L}{\nu}$	Ratio of inertial to viscous terms
Interaction parameter	N	$= \dfrac{\sigma L B_0^2}{\rho v_0}$	Ratio of electromagnetic to inertial terms
Hartmann number	Ha^2	$= h^2 B_0^2 \left(\dfrac{\sigma}{\rho \nu} \right)$	Ratio of electromagnetic to viscous terms

TABLE 1. Dimensionless parameters.

where the pressure gradient and the convective derivative have been neglected. The effect of the electromagnetic forces will be considered in a moment. Considering purely azimuthal flow, the only non-zero component is found to be

$$\frac{\partial v_\phi}{\partial t} = \nu \left(\frac{\partial^2 v_\phi}{\partial r^2} + \frac{1}{r} \frac{\partial v_\phi}{\partial r} - \frac{v_\phi}{r^2} \right). \tag{2.7}$$

We observe in passing that Taylor's solution, $\boldsymbol{v}(r) = (c_1 r + c_2/r)\hat{\boldsymbol{\phi}}$, satisfies both $\nabla^2 \boldsymbol{v} = 0$ and $\nabla \cdot \boldsymbol{v} = 0$ (Taylor 1923). The consequences of such non-dissipative velocity profiles will be addressed in more detail in §4.1. Some eddies, like those observed in these experiments, can be approximated by a piecewise sum of these non-dissipative solutions, but will undergo viscous damping near the point of transition. Heuristically, the time scale for dissipation of some feature of radius R can be derived by approximating

$$\frac{\partial \boldsymbol{v}}{\partial t} = \nu \nabla^2 \boldsymbol{v} \sim \frac{4\nu}{R^2} \boldsymbol{v}, \tag{2.8}$$

using the half-width of the radius of the eddy as a typical length scale for velocity gradients. This relation implies that viscous forces gradually smooth out the profile on the time scale of $\tau \approx R^2/4\nu$ for a laminar vortex (Aboelkassem, Vatistas & Esmail 2005). However, eddies within a turbulent vortex interact more strongly than a laminar sheared flow and ultimately smooth the velocity profile faster, increasing the effective viscosity, ν_{eff}, and decreasing τ. The process of representing turbulent diffusion as an effective viscosity is sometimes referred to as Boussinesq's hypothesis or an eddy-viscosity model, and ν_{eff} represents the addition of terms in the Reynolds stress tensor due to turbulent motion of the fluid (see Schmitt 2007).

Sommeria & Moreau (1982) pointed out that, at high Hartmann number and interaction parameter ($Ha \gg 1$ and $N \gg 1$), there is an additional term to account for Hartmann damping that should be included in (2.7). Namely,

$$\frac{\partial \boldsymbol{v}}{\partial t} = \nu \nabla^2 \boldsymbol{v} - \frac{B}{R} \left(\frac{\sigma \nu}{\rho} \right)^{1/2} \boldsymbol{v}. \tag{2.9}$$

The effect of this additional term was observed in some results for $N \gtrsim 5$ ($Ha \gtrsim 20$) and will be addressed in more detail in §4.3. Note that (2.9) was derived by Sommeria & Moreau (1982) for duct flow with two distinct Hartmann layers and consequently an additional factor of 2 was present in front of the additional damping term. However,

Parameter	Symbol	Value
Density	ρ	6361 kg m^{-3}
Kinematic viscosity	$\nu = \mu/\rho$	3.41×10^{-7} m^2 s^{-1}
Conductivity	σ	3.15×10^6 S m^{-1}

TABLE 2. Physical properties of $Ga_{67}In_{20.5}Sn_{12.5}$ alloy (Prokhorenko *et al.* 2000; Morley *et al.* 2008).

owing to the free surface in this experiment and the presence of only one Hartmann layer, the factor of 2 is removed for this scenario. For a detailed description of the roles of Hartmann layers and boundary conditions in MHD flows, (see Pothérat, Sommeria & Moreau 2005).

3. Experimental set-up

The experiments described in this paper were conducted in an acrylic (electrically insulating) channel 80 cm in length by 16 cm in width positioned horizontally in a uniform, vertical magnetic field perpendicular to the free surface of the fluid. A static silver-plated copper cylinder 19 mm in diameter was placed in the flow with its axis aligned with the magnetic field as illustrated in figure 1. The cylinder diameter corresponded to a blockage ratio of about 12 % and vortex interaction with the walls of the channel was minimal. The working fluid was a gallium–indium–tin eutectic described in table 2 that flowed through the channel with a mean depth of 1 cm at speeds between 14 and 18 cm s^{-1}. It should be noted that the channel was level with respect to gravity and the flow was due to a hydrostatic pressure gradient arising from the decrease in fluid surface height at the entrance to the outlet of the channel. Owing to the free surface, the fluid height varied slightly with flow rate and applied magnetic field due to the change in pressure required to maintain a constant flow rate. The flow was created with an Archimedes-style screw pump that acted as a constant displacement pump. As such, the volumetric flow rate was held constant within 5 % for a given set of experiments and the fluid height was free to adjust accordingly.

The entrance of the channel was designed to promote fully developed uniform flow and is described by Nornberg *et al.* (2008). The magnet consisted of an iron core to concentrate the magnetic flux created by a racetrack coil powered by a d.c. rectifier. The magnet produced a field intensity of up to 2.7 kG between pole faces, measuring 14 cm by 74 cm, separated by the experimental gap measuring 19 cm.

An array of 16 potential probes was inserted from the free surface into the core of the flow to make measurements of the induced electric potential as a proxy for the streamwise fluid velocity as seen in figure 1. The potential probes operated by measuring the local e.m.f. created from the motion of the conductive fluid through the applied magnetic field. The spatial resolution of the probes was limited to 4.5 mm (approximately $L/4$). The probe array was situated 60 cm downstream from the upstream edge of the iron core in order to eliminate effects arising from the fluid entering or exiting the magnetic field. At the location where the channel was situated with respect to the pole faces, the spatial variation in the magnetic field was less than 10 % in the cross-stream direction from the peak value at the centreline of the channel to the sidewalls and less than 1 % in the streamwise direction over the region of interest.
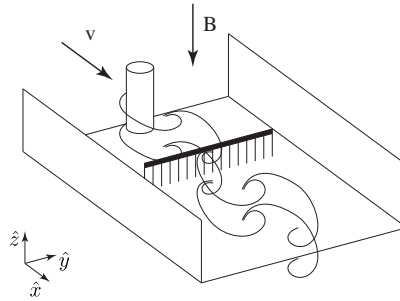
FIGURE 1. Experimental set-up showing vertical cylinder, potential probe array and magnetic field aligned with the axis of the cylinder.

Experiments were also conducted using an IR camera sensitive to wavelengths in the range of 2.5–5.1 µm to visualize the wake of a cylinder inserted into the flow from the free surface. Heat was injected via a resistive cartridge heater in contact with the surface of the metal upstream from the cylinder. The heater raised the fluid temperature by a few degrees to provide a tracer visible to the IR camera, but not enough to significantly drive flow directly (particularly because the system was buoyantly stable and Marangoni flows were not observed). The temperature of the fluid was then used as a passive scalar to track the fluid motion, which can be seen in the supplementary movie (available at http://dx.doi.org/10.1017/jfm.2014.11). These experiments demonstrated a considerable qualitative change in the nature of the wake of the cylinder as the interaction parameter was increased, and provided direct evidence of 'secondary vortices' as described by Wei & Smith (1986, p. 520) for small values of N. However, the physical contact of the heater with the surface of the metal unnecessarily complicated the shedding mechanism. To quantitatively describe the changes in the wake of the cylinder, the heater was removed and the fluctuations in the electric potential gradient (arising from velocity fluctuations) were directly sampled with the potential probes.

The operating principle of the potential probes can be derived from Ohm's law (2.2). As outlined by Müller & Bühler (2001) for quiescent laminar flows, the contribution to Ohm's law from the current density is $\boldsymbol{j}^* = 1/Ha\,\nabla \times \boldsymbol{b}^*$, where $\boldsymbol{b}^*$ is the non-dimensionalized induced magnetic field and $\boldsymbol{j}^* = \boldsymbol{j}/\sigma v_0 B_0$ is the dimensionless dimensionless current density. In the Hartmann layers, $\left|\nabla \times \boldsymbol{b}^*\right| \sim 1$, implying that $|\boldsymbol{j}/\sigma|/|\boldsymbol{v} \times \boldsymbol{B}| \sim 1/Ha$, but, in the core of the flow, $\left|\nabla \times \boldsymbol{b}^*\right| < 1$ due to the small gradient in the induced field. This can be calculated exactly by examining the analytic solution for flow through an insulating duct presented by Müller & Bühler (2001). By taking the curl of the solution for the induced magnetic field and solving for the magnitude of the current density in the core of the flow, it was found that $|\boldsymbol{j}/\sigma|/|\boldsymbol{v} \times \boldsymbol{B}| < 4\,\%$ at $Ha = 5$ and quickly falls below $1\,\%$ for $Ha \geqslant 10$. Others (see Sommeria 1986; Kljukin & Thess 1998; Sreenivasan & Alboussière 2002) have also discussed the error arising from internal currents on the measured potential gradient mentioned above, and concluded that, at sufficiently high Ha number, the effects are negligible.

The accuracy of the diagnostic in three-dimensional turbulent flows must also be considered. Owing to the turbulent nature of the flow at low N, significant currents can exist due to the interaction of velocity fluctuations with the background magnetic field. However, these currents are averaged out of the mean flow measurements, and the

fluctuations in the measured potential gradient can still be used to investigate velocity fluctuations by self-normalizing the signal from the probes, discussed in §4.1.

Once the flow becomes sufficiently quasi-two-dimensional ($N > 1$), the approximation that $j = 0$ can be used in (2.2), yielding $-\boldsymbol{E} \approx \boldsymbol{v} \times \boldsymbol{B}$. Using this approximation and replacing $\boldsymbol{E}$ with $-\nabla\phi$ from the electrostatic assumption, one obtains $\nabla\phi = \boldsymbol{v} \times \boldsymbol{B}$. Integrating over the distance between probe tips (chosen to lie in the proper orthogonal direction), the potential difference between two electrodes is found to be $\Delta\phi(v_x) = \overline{v_x}\, d B_z$, where $\overline{v_x} = (1/d) \int_0^d v_x(y)\, dy$. Experimentally, the averaged probe signals were found to be reliable for values of $Ha > 5$, corresponding to the lowest value of applied magnetic field for the work presented in this paper. The spatial averaging effect on the vortex profile due to the finite probe width was taken into account when fitting the velocity profiles, although this artifact was negligible in most cases.

Sequential experiments were conducted with the potential probe array located roughly 3, 5 and 14 diameters downstream from the cylinder. For each cylinder location, the magnetic field was scanned from a value of 150 to 2500 G, corresponding to a range of $0.01 \leqslant N \leqslant 8$ based on cylinder diameter and mean wake velocity, or $5 \leqslant Ha \leqslant 100$ as calculated based on the fluid depth. Time series from each of the probes (after amplification) were recorded at 1 kHz and the data logged via a PC. For each set of experiments at a fixed cylinder location, the volumetric flow rate was held constant and varied no more than 5 % as the magnetic field was scanned.

4. Results

The change in the nature of the wake of the cylinder as a function of N was studied through three sets of experiments. Two sets of experiments sampled the wake at 3 and 14 diameters downstream from the cylinder, with free-stream velocities of 14.0 and 13.9 cm s^{-1}, respectively. A third set of data was taken at five diameters into the wake, at a slightly higher fluid velocity of 17.8 cm s^{-1}, but still well within the shear-layer transition regime. The disruption of the flow due to the cylinder lowered the time-averaged velocity in the wake to 10.6, 13.5 and 11.6 cm s^{-1} for the cases of 3, 5 and 14 diameters, respectively. The ratio of the wake velocity to the free-stream velocity compared quite well with hydrodynamic results from Cantwell & Coles (1983), where $v_0/v_\infty \approx 0.76$. Throughout this section, data are only directly compared for experiments with a constant free-stream velocity, with one exception discussed in §4.3.

4.1. *Identification of vortices*

Individual vortices were identified in the wake by using the simultaneous measurements of the cross-stream profile of the electric potential (resulting from the streamwise velocity) to detect organized regions of circulation. In order to eliminate slight variations in calibration from one probe to another, and to remove the background flow from consideration, as done by Cantwell & Coles (1983), the potential probes were self-normalized to provide the most self-consistent picture of the streamwise velocity fluctuations across the channel. The background flow was approximated as the time average, $\langle v_x(y) \rangle$, over many vortex shedding cycles ($N_{cycles} > 100$) and the fluctuation amplitude was defined as

$$\xi(y, t) = \frac{v_x(y, t) - \langle v_x(y) \rangle}{\langle v_x(y) \rangle} \times 100. \qquad (4.1)$$
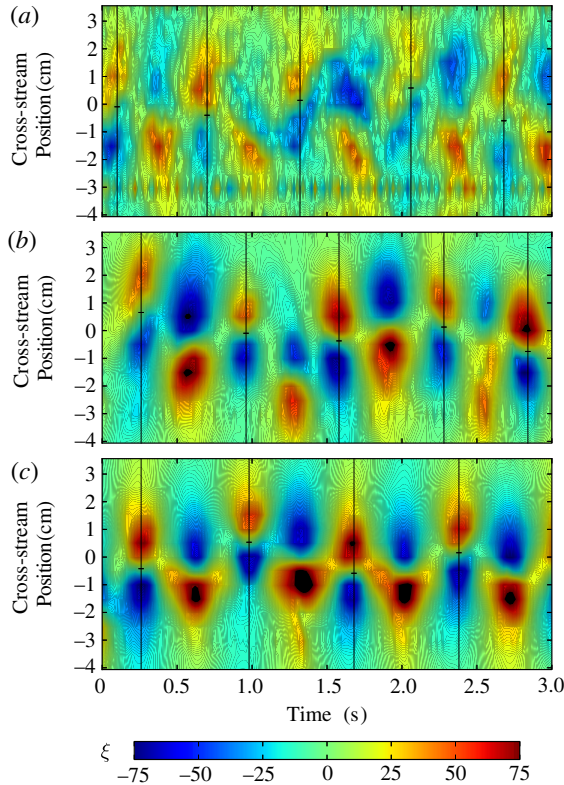
FIGURE 2. Contours of fluctuations in measured potential in the wake approximately three diameters behind the cylinder as a function of cross-channel position and time at (*a*) $N = 0.01$, (*b*) $N = 0.66$ and (*c*) $N = 1.85$.

Vortices in the wake of the cylinder were visualized by examining ξ as a function of cross-stream position and time, as plotted in figure 2, where each pair of lobes represents a vortex passing the fixed probe array in time. Over the entire scan in magnetic field, a clear von Kármán street was observed by the potential probe array as expected from the preliminary IR measurements.

Since the measurement from the potential probes only captures the streamwise component of the velocity, $\xi(y, t)$ only represents the azimuthal velocity of a vortex when the centre of the vortex is aligned with the probe array as it is advected downstream. Additionally, the position of the vortex in the cross-stream direction must also be located in order to define the centre of rotation, where $r = 0$. Therefore, each vortex must be found in two dimensions: time and cross-stream position.

In order to locate the centre of the vortex in time, local maxima of the root mean square, r.m.s. $= (\int |\xi(y, t)|^2 \, \mathrm{d}y)^{1/2}$, of the measured velocity profile were found. This time coincides with the point when the centre of rotation of the vortex was directly in line with the probe array and ξ exactly matches the azimuthal component of the vortex velocity. The maxima in time are indicated in figure 2 by vertical lines (only shown for vortices with clockwise rotation, i.e. those with negative vorticity). Once the vortex probe crossing time was found, the zero-crossing point of the ξ profile was identified with a linear interpolation of the two velocity measurements nearest
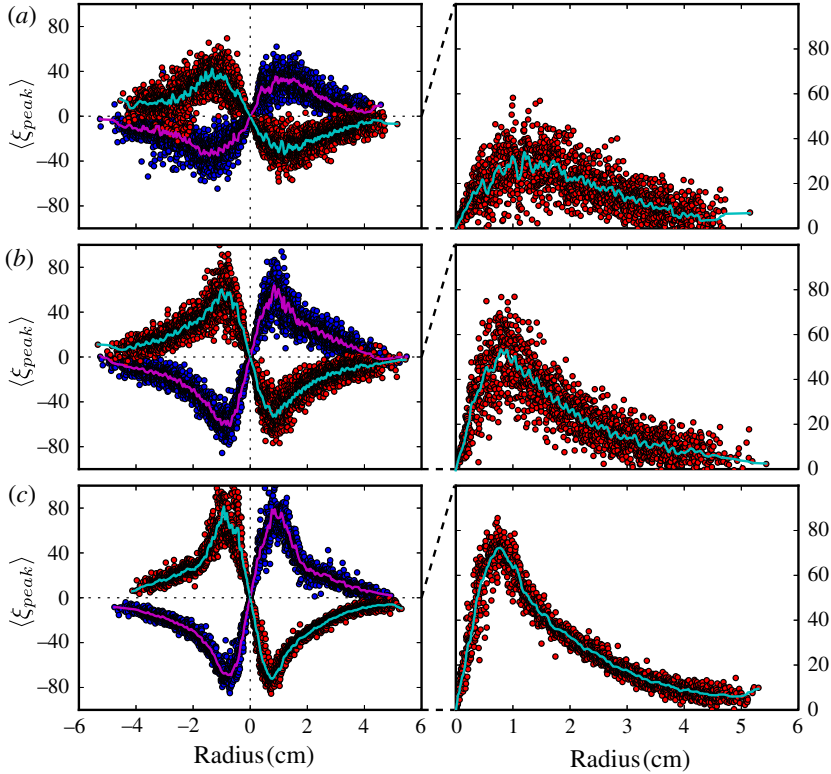
FIGURE 3. (Colour online) Velocity profiles of vortices with positive (red) and negative (blue) vorticity at (*a*) low $N = 0.01$, (*b*) moderate $N = 0.66$ and (*c*) high $N = 1.85$ interaction parameter, as a function of radius. Profiles correspond to contours in figure 2 at three diameters into the wake. The panels in the right column correspond to quadrant IV of the panels in the left column, to highlight the finer structure within the profiles.

the centre of rotation. This point indicated the location of the vortex in the cross-stream direction and is shown in figure 2 by horizontal dashes. The coordinates of the velocity profile were then shifted such that $r = 0$ corresponded to the point where $\xi = 0$. If any vortices did not meet the criteria for selection, that is, if the local maximum of the r.m.s. was ambiguous or the centre of the vortex fell near the edge of the probe array, the vortex was neglected and excluded from the aggregate profile.

The key advance to the approach outlined above was using the random location of the shed vortices (in the cross-stream direction) to produce a statistical collection of velocity profiles, allowing for the calculation of an ensemble-averaged vortex velocity profile. As the streamlines reconnected and each vortex separated from the cylinder, the centre of the shed vortex was slightly displaced by a distance δ from the centreline of the channel. Moreover, at high Reynolds number, δ fluctuated randomly. Therefore, as the shed vortex was advected through the fixed probe array, the diagnostic was able to sample the internal velocity profile of each vortex at a slightly different location. By identifying the centre of each vortex and shifting the measured profile accordingly, a well-resolved internal velocity profile was obtained. The result can be seen in figure 3, which shows the aggregate velocity profiles corresponding to the vertical lines seen in figure 2.

As can be seen in the left column of figure 3, the velocity profiles corresponding to vortices of positive and negative vorticity are indistinguishable, and the profiles show strong symmetry about the origin, with one subtle exception. Note that, for vortices of both directions of rotation, the side of the vortex supplementing the streamwise velocity (quadrants I and II) developed a distinct 'kink' in the velocity profile as the magnetic field was increased. The cause of this feature is currently unknown, though it was observed in the velocity profiles at all three downstream positions.

4.2. *Vortex characteristics*

By implementing the technique described in §4.1, an ensemble of velocity profiles was collected. The average of the ensemble was assumed to be representative of the average vortex for a given field strength and can be seen as the solid curves in figure 3. For $N \gtrsim 0.5$, the effects of the magnetic field on the vortices and the measured spectral slopes of the power spectra of the fluctuations were experimentally observed to saturate, in agreement with results from other experiments in various geometries mentioned previously (see Harris 1960; Lahjomri *et al.* 1993; Mück *et al.* 2000; Branover *et al.* 2004).

The velocity profiles shown in the right column of figure 3 are the upstream component of vortices with positive vorticity (quadrant IV of the left column). Given that vortices of positive and negative vorticity showed no discernible difference for a given vortex street (other than their sign), they were combined when discussing trends in radius, rotation and circulation to increase the number of measurements used in the analysis.

At low values of the applied magnetic field ($N \leqslant 0.5$), the measured azimuthal velocity profile varied considerably, as seen in figure 3(*a*,*b*), which is likely to be due to the presence of small-scale turbulent eddies. However, by identifying at least 150 vortices of both positive and negative vorticity, an average profile was calculated. At higher field strengths, it was observed that vortices become much more regular and coherent, resulting in a very clear radial velocity profile with very little deviation, as shown in figure 3(*c*). Dousset & Pothérat (2012) and Andreev *et al.* (2013) also observed a similar stabilization of the wake at higher applied magnetic fields.

The presence of small-scale turbulent eddies within the vortices was investigated by examining the spread of the ensemble relative to the average velocity profile of the vortex, $\langle \xi \rangle$. At low fields, the individual velocity profiles have significant deviations from the averaged profile, indicative of irregular, turbulent fluctuations on top of the global rotation. One metric for the coherence of the vortex, and by extension the absence of eddies, is the scaled variance of the ensemble over the smoothed profile, $\chi^2 = \sum [\xi(r_i) - \langle \xi \rangle(r_i)]^2 / \sum \langle \xi \rangle^2(r_i)$. Above a threshold in the interaction parameter near $N \approx 0.5$, the fluctuations on top of the global rotation were dramatically reduced, as seen in figure 4.

The claim that χ^2 is related to the presence of small-scale features can be explained as follows. As described in §1 and visualized in the supplementary IR movie mentioned above, a turbulent wake at $N \ll 1$ consists of many randomly oriented eddies within the flow. As these eddies pass through the probe array, they alter the local measurement. For instance, if an eddy with vorticity parallel to the cylinder axis happened to be centred directly in line with one electrode of the probe array when it passed through the diagnostic, then the measured velocity of the electrode pair on one side would report a velocity slightly higher than the overall tangential speed of the vortex, while the electrode pair on the other side would report a velocity slightly
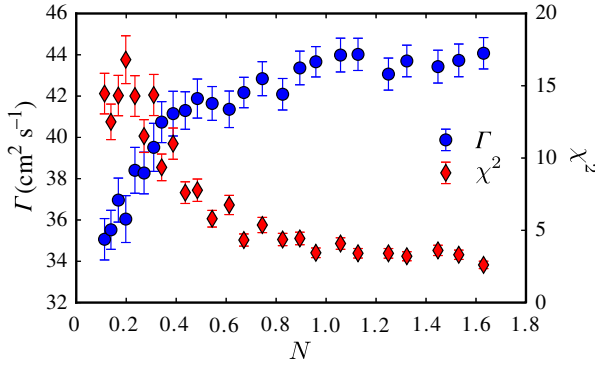
FIGURE 4. (Colour online) Total circulation Γ and chi-squared value χ^2 of measured profiles over the average profile versus interaction parameter N five diameters into wake.

lower. Statistically, these eddies average out and produce a reliable mean velocity profile, though the standard deviation from that mean is related to the number and magnitude of eddies present in the flow.

In order to quantify changes in the overall vortex structure in the wake of the cylinder as N was increased, the averaged vortex velocity profiles were fitted to a Rankine vortex velocity profile. This vortex model consists of a core with constant angular velocity surrounded by a free vortex. The velocity profile in a coordinate system centred at centre of rotation for a Rankine vortex is given by $v_r = v_z = 0$ and

$$v_\phi(r) = \begin{cases} \Gamma r/(2\pi R^2), & r \leqslant R, \\ \Gamma/(2\pi r), & r > R, \end{cases} \tag{4.2}$$

where $\Gamma = \oint v_\phi \, \mathrm{d}s = 2\pi\omega R^2$ is the circulation of a vortex of radius R and angular velocity ω. Observe that the Rankine profile in both domains is represented by a Taylor solution, described following (2.7). By fitting the experimental profiles to this model vortex, it was possible to examine the effect of the magnetic field on vortex parameters, including the core rotation rate ω, vortex radius R and circulation Γ.

Figure 4 also shows the measured circulation as a function of interaction parameter. As N is increased towards unity, the prevalence of three-dimensional small-scale features is reduced, in agreement with the simulations by Kanaris *et al.* (2013), resulting in an increase in measured circulation. For $N > 2$, Hartmann damping alters the fluid motion and causes the circulation to decrease. Both of these regimes can be seen in figure 5.

Near the hydrodynamic regime, the presence of small-scale three-dimensional eddies acts to rapidly diffuse the angular momentum of the vortex and facilitate vortex breakdown (resulting in less global circulation). The aforementioned eddy-damped model for turbulence reviewed by Schmitt (2007) can be applied for hydrodynamic flows to model this behaviour. For MHD turbulence, Thess & Zikanov (2007) discuss the stability of a triaxial ellipsoid in the presence of an applied magnetic field, and consider the growth of a perturbation as a function of the interaction parameter. In particular, Thess & Zikanov (2007) showed that structures become unstable when the interaction parameter of the ellipsoid, $N_\omega = \sigma B^2/\rho W$ (where W is the vorticity of the structure), falls below the critical value of $N_c = 1$. Accounting for the different definitions of N, the transition in this work was observed to occur near $N_\omega \approx 1$. This
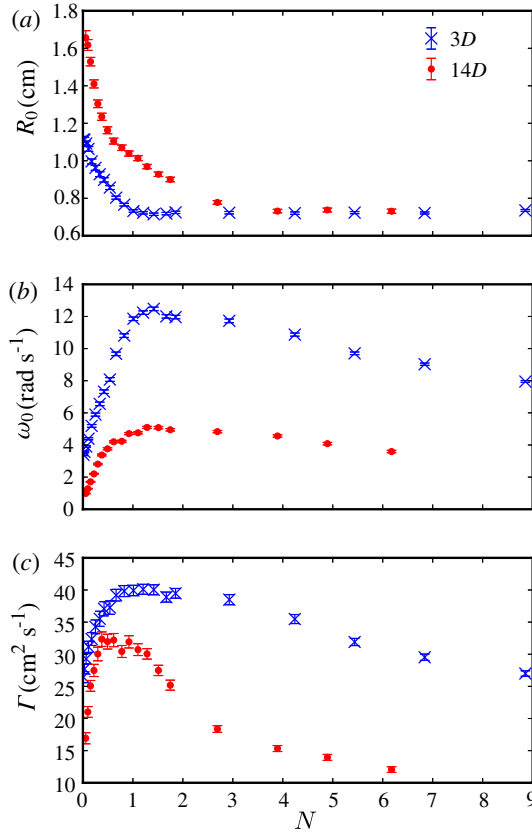
FIGURE 5. (Colour online) Trends of vortex (*a*) radius, (*b*) rotation and (*c*) circulation versus interaction parameter at three and 14 diameters into the wake.

agrees with the observations that, at low N, the wake of the cylinder is unstable. Thess & Zikanov (2007) also examine the stability of a two-dimensional strained elliptical vortex, which would be applicable to perfectly collimated vortices. In general, the stability of the vortices is dependent on N_ω, not the global N. However, the stability of these coherent vortices is not a significant concern, owing to their low eccentricity and moderate interaction parameter.

Secondly, many eddies smaller than the spatial resolution of the velocimetry diagnostic would exist in a hydrodynamic flow at this Reynolds number and would contain a small but finite amount of angular momentum not captured by the diagnostic. These small-scale features result from both the turbulent cascade and the instability of the boundary layer of the cylinder as discussed by Wei & Smith (1986, pp. 519–521). In both cases, the eddies possess vorticity aligned with that of the vortex, and the smallest scale length is dictated by the interaction of the bulk flow with the boundary layers. Since the circulation is essentially a metric for the total angular momentum of the vortex, and the (hydrodynamic) Kolmogorov length scale for these flows can be estimated to be $\eta = L/Re^{3/4} \approx 25$ μm (Frisch 1995), the measured circulation would not capture the rotation present in these small-scale features. This limitation would result in a measured circulation that was artificially depressed at $N < 0.5$. This can be visualized by considering an eddy with a diameter less than the probe
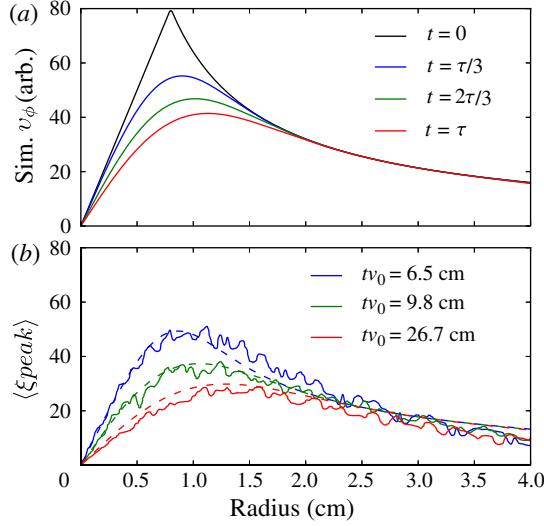
FIGURE 6. Viscous vortex damping seen in (*a*) simulation of Rankine profile with $\tau = R^2/4\nu$, and (*b*) radial velocity profiles at $N = 0.4$ (0.7 kG) at three positions downstream in the wake. Dashed lines represent the best-fitting profiles from the simulations.

width and vorticity parallel with the cylinder axis passing directly between two electrodes. Because the probes only report the average velocity, the eddy's upstream velocity component would exactly cancel its downstream component, and the probe measurement would have no way of quantifying the motion (and circulation) of the eddy itself.

As seen in figure 5(*a*,*b*), at low magnetic fields the rotation rate of the vortices increases linearly with the field, while the radius of the core decreases to about 7.5 mm (or 0.4 d) as the interaction parameter approaches unity. As N was increased above 2, Hartmann braking introduced in (2.9) began to damp the rotation of the vortices, explaining the roll-off of the rotation rate and circulation at the higher field strengths. This can be seen in figure 5(*b*,*c*), which shows the rotation rate and the global angular momentum reduced. The trend in the vortex radius as a function of interaction parameter is quite similar to that found by Sommeria (1988), in which the evolution of an electrically driven isolated vortex was studied, and the radius of the 'core vortex' was found to decrease with increasing N_ω, as in the current work.

4.3. *Vortex decay*

Analytically, the viscous damping of a Rankine profile can be seen by noting that each region of the Rankine vortex model in (4.2) is a Taylor solution, as discussed in § 2, and are therefore undamped by viscosity. However, the discontinuous derivative at $r = R$ of the Rankine profile results in a non-zero value of the Laplacian at the transition, resulting in local damping. As the vortex viscously damps, the profile deviates from the constituent Taylor solutions, and thereby undergoes further damping away from the peak. This can be seen in figure 6(*a*), which shows the numerical solution to the evolution of an ideal Rankine vortex.

For a fixed flow velocity and location in the wake, the measured profiles were observed to be far less damped for $N \gtrsim 1$ than for $N < 1$. This is clearly illustrated

in figure 3(*a*,*c*), where the vortex three diameters into the wake is much less damped at the higher magnetic field from the lack of turbulent dissipation. As also proposed by Kanaris *et al.* (2013), the change was most likely a result of the magnetic field reducing the prevalence of small-scale turbulent structures in the flow, thereby decreasing the effective viscosity and subsequent damping of the velocity profile. Once the vortex profiles were collected at three positions in the wake of the cylinder, it was possible to artificially examine the spatiotemporal decay of the vortices as a function of the applied magnetic field.

For hydrodynamic flows, it has been shown by Roshko (1954) and later by Cantwell & Coles (1983) that the circulation of vortices divided by the free-stream velocity was constant for a given geometry. This is equivalent to the statement that vorticity in the wake of the cylinder is linearly dependent on the fluid velocity. Therefore, by looking only at normalized profiles, the results from each of the three cylinder locations were compared over the range $0.01 < N < 2$, despite the slightly different v_∞. Based on this assumption, the normalized vortex amplitude, ξ_{peak}, for the five-diameter case was included when examining the decay of the profiles and calculating the 'effective viscosity'. It should be noted that the inclusion of the five-diameter case changed the measured value of v_{eff} by less than 10 % for all field strengths.

The average fluid velocity in the wake, v_0, was used to infer the time from inception of the vortices until they passed the probe array. This approach made it possible to examine the evolution of the velocity profile for each field strength as seen in figure 6(*b*). These sequential profiles were then used to calculate the effective viscosity. First, a relaxed Rankine profile was fitted to the experimental profile at three diameters into the wake. This profile was iteratively compared to simulated profiles evolving according to (2.7) with varying radii as a function of time, as seen in figure 6(*a*). After identifying the best-fitting simulated profile (in radius R_0, time t_0 and amplitude Γ_0) for the experimental measurements made three diameters into the wake, the experimental profiles from 5 and 14 diameters downstream were then fitted in a similar manner to the temporal decay of the same seed vortex of fixed radius and amplitude, R_0 and Γ_0, to find the times, t_1 and t_2, corresponding to the best-fitting relaxed profile. While the supplementary IR movie seems to indicate that vortices form immediately behind the cylinder, in order to remove the uncertainty of the exact shedding position, the initial time t_0 found from the three-diameter location was subtracted from the subsequent times t_1 and t_2 in order to define the simulated time, t_{sim}. The effective viscosity was calculated for the 5- and 14-diameter locations through the ratio of the simulated time t_{sim}, corresponding to the best fit, to the experimental time t_{exp}, extracted from the location of the cylinder relative to the probes and fluid velocity of the wake, v_0. That is,

$$t_{sim} = \alpha \frac{R^2}{4v}, \quad t_{exp} = \alpha \frac{R^2}{4v_{eff}}, \quad \frac{v_{eff}}{v} = \frac{t_{sim}}{t_{exp}}, \tag{4.3}$$

where α merely represents the fraction of the time constant that has elapsed. Figure 7 shows the effective viscosity decreasing as $N^{-0.49\pm0.04}$ over a range corresponding to $0.1 \leqslant N \leqslant 1.7$, before Hartmann damping of the vortices became prevalent. It should be noted that this scaling may be case-specific, and future experiments with various cylinder diameters, flow rates, etc. would be useful for evaluating the universality of the relationship.

Despite signs of damping at $N > 2$, the electromagnetic damping term in (2.9) was neglected when comparing the decay of the experimental profiles. First of all, the
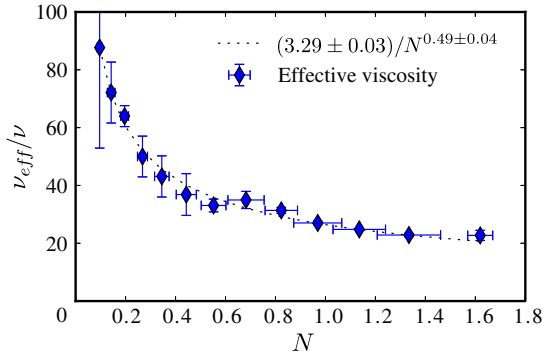
FIGURE 7. (Colour online) Effective viscosity as a function of interaction parameter.

derivation of (2.9) was based on the assumption that $N \gg 1$ and therefore its validity for N near unity is not guaranteed. Further, only viscous damping broadens the velocity profile and accounts for the outward shift in the peak velocity observed in figure 6. The experimental data indicated an outward shift in the maximum velocity as the amplitude decays, but does not show any evidence of a linear damping term that would act to scale the velocity proportionally across the profile. The effective viscosity was only calculated for $N < 2$ in this work and Hartmann damping was not experimentally observed at $N \leqslant 2$ as seen in figures 4 and 5, which show no appreciable decrease in the circulation over the range $0.5 < N < 2$, compared to the significant decrease in Γ for $N > 2$ seen in figure 5. For these reasons, only turbulent viscous damping described in (2.7) was considered when examining the decay of the vortices.

As mentioned in §1 and discussed by Eckert *et al.* (2001) and Ueno & Moreau (2006), three-dimensional features are expected to be damped out by the magnetic field on the Joule time scale, τ_J, while two-dimensional vortices are expected to be ohmically damped on the Hartmann time scale at large N, $\tau_{Ha} = Ha\,\tau_J$. Since $\tau_J \approx 0.05$ s at $N \approx 4$ and $Ha \approx 70$, $\tau_{Ha} \approx 3.5$ s, Hartmann damping was a significant effect for the 14-diameter case, but Joule damping was dominant on short time scales and was the primary modifier of the rotation profile at three and five diameters downstream. That is, for the three- and 14-diameter cases, vortices in the wake evolved for approximately 0.5 and 2 s, respectively, as they were advected downstream to the measurement location. This difference in time as compared to the Hartmann time scale explains why the circulation for the 14-diameter case falls off much more significantly than the three-diameter case in figure 5(*c*) as a function of N.

4.4. *Dependence of fluctuation spectra on* **B**

A change in spectral slope was observed in these experiments by looking at the power spectral density (PSD) of the velocity fluctuations as seen in figure 8. Taylor's hypothesis was employed to relate ω and k in order to obtain the energy spectra as a function of wavenumber from time series of velocity fluctuations.

By fitting the slope of the PSD, the power-law exponent was observed to transition from a Kolmogorov-like hydrodynamic state with a near $k^{-5/3}$ power law for $N \ll 1$ to a $k^{-3.5}$ power law as N was increased for all positions in the wake seen in figure 9. This agrees with other evidence of the transition of the flow presented in
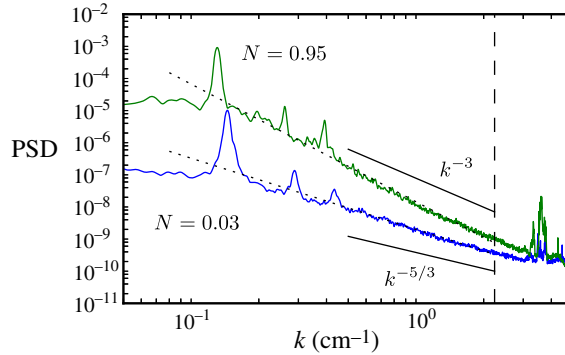
FIGURE 8. (Colour online) Power spectra of probe signal from three diameters into the wake at two values of N. Dotted lines indicate fit used to extract the power-law scaling. The vertical dashed line represents the spatial resolution limit of the probes.
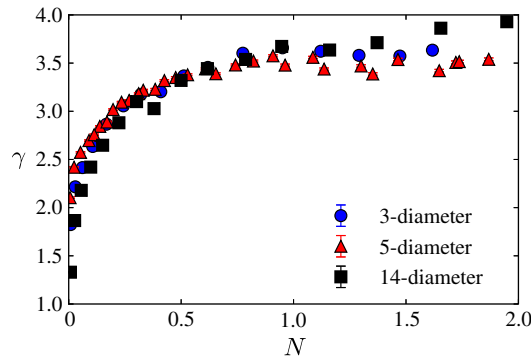

FIGURE 9. (Colour online) Spectral slope ($k^{-\gamma}$) of power spectra versus N, showing smooth transition from hydrodynamic to MHD state for all three positions in the wake.

this paper, as well as the change in spectral slope of velocity fluctuations observed in other experiments over a similar range in N (Sommeria 1986; Eckert *et al.* 2001). It should be noted that the spatial resolution of the probes was insufficient to resolve the inertial range of the energy spectrum, and, as such, definitive conclusions regarding the presence or absence of an inverse cascade or the dimensionality of the flow from the spectra cannot be made. However, the change in the spectral slope clearly indicated a quantifiable transition in the energy distribution. The large peak of both curves near $k = 0.1$ in figure 8 represents the primary shedding frequency and illustrates the lack of dependence of the shedding mechanism on the magnetic field for these values of interaction parameter. The Strouhal number, a non-dimensional frequency defined as $St = fd/v_\infty$, where again d is the cylinder diameter, f is the shedding frequency and v_∞ is the free-stream fluid velocity, was observed to vary less than 10 % from 0.2 as the field strength was increased.

5. Conclusions

The internal velocity profiles of vortices shed from a vertical cylinder were presented as a function of the applied vertical magnetic field. A novel approach

for isolating azimuthal velocity profiles of these vortices was developed, and from these velocity profiles the effects of the magnetic field on the internal dynamics of vortices were inferred.

The radii of vortices were observed to decrease with applied magnetic field due to a reduction in the effective viscosity as a result of the magnetic field altering small-scale eddies. Meanwhile, the rotation rate of the vortices for values of interaction parameter in the range of $0 \leqslant N < 2$ was observed to increase. At $N > 2$, Hartmann braking damped the motion of the vortices, resulting in a reduction in the total circulation, Γ. However, electromagnetic damping of the motion was not observed to be significant for $N < 2$.

The prevalence of small-scale turbulent features has been experimentally shown to decrease significantly as N approaches 0.5. Above this threshold, the magnetic field alters the evolution of the eddies, as evidenced by both the decrease in the χ^2 of the measured velocity profiles and in the significant reduction of the effective viscosity, ν_{eff}.

Measurements of the velocity fluctuations in the wake of a cylinder at moderate *Re* manifest a clear change in spectral slope indicating the transition from one state to another. This transition in the spectral slope was also observed to occur as N approached 0.5, coinciding with the transition observed with other metrics. Further, there was a noticeable absence of small-scale features in magnetized cases from both IR observations and potential probe measurements.

By examining the decay of the vortices, it was found that the effective viscosity scaled like $N^{-0.49 \pm 0.04}$ for these experiments. The stabilizing effect of the magnetic field as discussed by Thess & Zikanov (2007) is thought to be the most probable explanation for the significant reduction in effective viscosity.

It is evident that the imposed magnetic field introduces a strong anisotropy for the vorticity of vortices within the fluid, which results in macroscopic behaviour significantly different from that without a magnetic field.

Acknowledgements

Supplementary movie

A supplementary movie is available at http://dx.doi.org/10.1017/jfm.2014.11.

REFERENCES

ABOELKASSEM, Y., VATISTAS, G. H. & ESMAIL, N. 2005 Viscous dissipation of Rankine vortex profile in zero meridional flow. *Acta Mechanica Sin.* **21**, 550–556.

ALBOUSSIÈRE, T., USPENSKI, V. & MOREAU, R. 1999 Quasi-2D MHD turbulent shear layers. *Exp. Therm. Fluid Sci.* **20**, 19–24.

ALEMANY, A., MOREAU, R., SULEM, P. L. & FRISCH, U. 1979 Influence of an external magnetic field on homogeneous MHD turbulence. *J. Méc.* **18** (2), 277–313.

ANDREEV, O., KOLESNIKOV, Y. & THESS, A. 2013 Visualization of the Ludford column. *J. Fluid Mech.* **721**, 438–453.

BRANOVER, H., EIDELMAN, A., GOLBRAIKH, E., KAPUSTA, A. & MIKHAILOVICH, B. 2004 Wave–mean flow interaction in an MHD wake behind bluff body. *Fluid Dyn. Res.* **35**, 287–298.

CANTWELL, B. & COLES, D. 1983 An experimental study of entrainment and transport in the turbulent near wake of a circular cylinder. *J. Fluid Mech.* **136** (1), 321–374.

DAVIDSON, P. A. 1997 The role of angular momentum in the magnetic damping of turbulence. *J. Fluid Mech.* **336**, 123–150.

DAVIDSON P. A. (Ed.) 2001 *An Introduction to Magnetohydrodynamics*. Cambridge University Press.

DOUSSET, V. & POTHÉRAT, A. 2008 Numerical simulations of a cylinder wake under a strong axial magnetic field. *Phys. Fluids* **20**, 017104.

DOUSSET, V. & POTHÉRAT, A. 2012 Characterization of the flow past a truncated square cylinder in a duct under a spanwise magnetic field. *J. Fluid Mech.* **691**, 341–367.

ECKERT, S., GERBETH, G., WITKE, W. & LANGENBRUNNER, H. 2001 MHD turbulence measurements in a sodium channel flow exposed to a transverse magnetic field. *Intl J. Heat Fluid Flow* **22** (3), 358–364.

FRANK, M., BARLEON, L. & MÜLLER, U. 2001 Visual analysis of two-dimensional magnetohydrodynamics. *Phys. Fluids* **13** (8), 2287–2295.

FRISCH U. (Ed.) 1995 Cambridge University Press.

HARRIS L. P. (Ed.) 1960 *Hydromagnetic channel flows*. Technology Press, MIT.

KANARIS, N., ALBETS, X., GRIGORIADIS, D. & KASSINOS, S. 2013 Three-dimensional numerical simulations of magnetohydrodynamic flow around a confined circular cylinder under low, moderate, and strong magnetic fields. *Phys. Fluids* **25**, 074102.

KLEIN, R. & POTHÉRAT, A. 2010 Appearance of three dimensionality in wall-bounded MHD flows. *Phys. Rev. Lett.* **104**, 034502.

KLEIN, R., POTHÉRAT, A. & ALFERENOK, A. 2009 Experiment on a confined electrically driven vortex pair. *Phys. Rev.* **79**, 016304.

KLJUKIN, A. & THESS, A. 1998 Direct measurement of the stream-function in a quasi-two-dimensional liquid metal flow. *Exp. Fluids* **25**, 298–304.

KNAEPEN, B. & MOREAU, R. 2008 Magnetohydrodynamic turbulence at low magnetic Reynolds number. *Annu. Rev. Fluid Mech.* **40**, 25–45.

KOLESNIKOV, Y. B. & TSINOBER, A. B. 1972 Two-dimensional turbulent flow behind a circular cylinder. *Magn. Gidrodin.* **3**, 23–31 (translation in *Magnetohydrodynamics* **8**, 300–307).

KOLESNIKOV, Y. B. & TSINOBER, A. B. 1974 Experimental investigation of two-dimensional turbulence behind a grid. *Isv. Akad. Nauk. SSSR Mekh. Zhidk. Gaza* **4**, 146–150 (translation in *Fluid Mech.* **4**, 621–624).

KOLMOGOROV, A. N. 1941 The local structure of turbulence in incompressible viscous fluid for very large Reynolds' numbers. *Dokl. Akad. Nauk SSSR* **30** (4), 299–303 (reprinted in *Proc. R. Soc. Lond.* A **434**, 9–13).

KRAICHNAN, R. H. 1967 Inertial ranges in two-dimensional turbulence. *Phys. Fluids* **10** (7), 1417–1423.

KRAICHNAN, R. H. 1971 Inertial-range transfer in two- and three-dimensional turbulence. *J. Fluid Mech.* **47** (3), 525–535.

LAHJOMRI, J., CAPÉRAN, P. & ALEMANY, A. 1993 The cylinder wake in a magnetic field aligned with the velocity. *J. Fluid Mech.* **253**, 421–448.

MORLEY, N. B., BURRIS, J., CADWALLADER, L. C. & NORNBERG, M. D. 2008 GaInSn usage in the research laboratory. *Rev. Sci. Instrum.* **79** (5), 056107.

MÜCK, B., GÜNTHER, C., MÜLLER, U. & BÜHLER, L. 2000 Three-dimensional MHD flows in rectangular ducts with internal obstacles. *J. Fluid Mech.* **418**, 265–295.

MÜLLER, U. & BÜHLER, L. 2001 *Magnetofluiddynamics in Channels and Containers*. Springer.

NORNBERG, M. D., JI, H., PETERSON, J. L. & RHOADS, J. R. 2008 A liquid metal flume for free surface magnetohydrodynamic experiments. *Rev. Sci. Instrum.* **79**, 094501.

PAPAILIOU, D. & LYKOUDIS, P. 1974 Turbulent vortex streets and the entrainment mechanism of the turbulent wake. *J. Fluid Mech.* **62**, 11–31.

POTHÉRAT, A., SOMMERIA, J. & MOREAU, R. 2005 Numerical simulations of an effective two-dimensional model for flows with a transverse magnetic field. *J. Fluid Mech.* **534** (1), 115–143.

PROKHORENKO, V. Y., ROSHCHUPKIN, V. V., POKRASIN, M. A., PROKHORENKO, S. V. & KOTOV, V. V. 2000 Liquid gallium: potential uses as a heat-transfer agent. *High Temp. USSR* **38** (6), 954–968.

ROSHKO, A. 1954 On the development of turbulent wakes from vortex streets. *NACA TN* 3169.

SCHMITT, F. G. 2007 About Boussinesq's turbulent viscosity hypothesis: historical remarks and a direct evaluation of its validity. *C. R. Méc.* **335** (9), 617–627.

SOMMERIA, J. 1986 Experimental study of the two-dimensional inverse energy cascade in a square box. *J. Fluid Mech.* **170**, 139–168.

SOMMERIA, J. 1988 Electrically driven vortices in a strong magnetic field. *J. Fluid Mech.* **189**, 553–569.

SOMMERIA, J. & MOREAU, R. 1982 Why, how, and when, MHD turbulence becomes two-dimensional. *J. Fluid Mech.* **118**, 507–518.

SREENIVASAN, B. & ALBOUSSIÈRE, T. 2002 Experimental study of a vortex in a magnetic field. *J. Fluid Mech.* **464**, 287–309.

STROUHAL, V. 1878 Ueber eine besondere Art der Tonerregung. *Ann. Phys. Chem.* **5** (10), 216–251.

TABELING, P. 2002 Two-dimensional turbulence: a physicist approach. *Phys. Rep.* **362** (1), 1–62.

ATAYLOR, G. I. 1923 Stability of a viscous liquid contained between two rotating cylinders. *Phil. Trans. R. Soc. Lond.* **223**, 289–343.

THESS, A. & ZIKANOV, O. 2007 Transition from two-dimensional to three-dimensional magnetohydrodynamic turbulence. *J. Fluid Mech.* **579**, 383–412.

UENO, K. & MOREAU, R. 2006 Damping rate of magnetohydrodynamic vortices at low magnetic Reynolds number. *Phys. Fluids* **18**, 025105.

VAN DYKE M. (Ed.) 1982 *An Album of Fluid Motion*. Parabolic Press.

WEI, T. & SMITH, C. R. 1986 Secondary vortices in the wake of circular cylinders. *J. Fluid Mech.* **169**, 513–533.

WILLIAMSON, C. H. K. 1996 Vortex dynamics in the cylinder wake. *Annu. Rev. Fluid Mech.* **28**, 477–539.

WILLIAMSON, C. H. K., WU, J. & SHERIDAN, J. 1995 Scaling of streamwise vortices in wakes. *Phys. Fluids* **7** (10), 2307–2309.

ZIKANOV, O. & THESS, A. 1998 Direct numerical simulation of forced MHD turbulence at low magnetic Reynolds number. *J. Fluid Mech.* **358**, 299–333.